Flow focusing with miscible fluids in microfluidic devices

Gemma Houston, Paolo Capobianchi and Mónica S. N. Oliveira

James Weir Fluids Laboratory, Department of Mechanical and Aerospace Engineering, University of Strathclyde, Glasgow G1 1XJ, UK

ABSTRACT

In this work, a series of experiments and numerical simulations performed using a Volume-of-Fluid approach were carried out to investigate the flow of miscible viscous fluid systems through microfluidic flow focusing devices with one central inlet stream (with 'Fluid 1') and two lateral inlet streams (with 'Fluid 2'). The combined effect of the fluid viscosity ratio and the inlet velocity ratio on the characteristics of the central focused outlet stream was assessed in microfluidic channels with different aspect ratios. An analytical expression for the two-dimensional case, relating the width of the central focused stream in the outlet channel with the velocity ratio and the viscosity ratio, was also derived from first principles. The analytical results are in excellent agreement with the two-dimensional numerical results, and the expression is also able to represent well the experimental findings for the configuration with an aspect ratio of 0.84. The width of the central focused outlet stream at the centre plane is seen to decrease with both the velocity ratio and the viscosity ratio. The results of the three-dimensional numerical simulations and experimental measurements are in good agreement, producing further insight into the curved interface known to exist when high viscosity contrasts are present in parallel flow systems. It was observed that the interface curvature across the depth of the channel cross section is strongly dependent on the ratio of inlet viscosities and microchannel aspect ratio, highlighting the 3D nature of the flow, in which confinement plays a significant role.

This is a peer-reviewed, accepted author manuscript of the following article: Houston, G., Oliveira, M. S. N., & Capobianchi, P. (2022). Flow focusing with miscible fluids in microfluidic devices. Physics of Fluids. https://doi.org/10.1063/5.0118087

I. INTRODUCTION

Hydrodynamic flow focusing at the microscale has been adopted in a number of practical applications that require bringing multiple fluids into contact, such as microfluidic mixing (Knight et al. 1998, Nguyen and Huang 2005), droplet formation (Cubaud et al. 2005), cell analysis (Ateya et al. 2008) and in the microfabrication of fibres, known as microfluidic spinning (Lan et al. 2009, Daniele et al. 2015). Microfluidic spinning has sparked interest over the past few decades with the ability to fabricate fibres of diverse shapes and sizes without the requirement for complex machinery (Jun et al. 2014). Improving the level of control and manipulation of fluids within these devices is key for the production of well defined, predictable, tuneable fibres according to their specific purpose (Lee et al. 2006, Ateya et al. 2008).

Typical flow focusing devices consist of a cross shaped microchannel with three fluid inlets (a central inlet stream with Fluid 1 and two lateral streams with Fluid 2 as shown in Figure 1) and a longer outlet channel, in which a central focused stream is produced. Different design configurations, in which lateral streams confine and shape a central fluid stream, have been used depending on the application. These include simple configurations with lateral perpendicular (cf. Figure 1c) or angled inlets (cf. Figure 1b) relative to the central inlet stream (Cubaud and Mason 2008, Oliveira et al. 2012), or more complex configurations with additional geometrical features, where e.g. an orifice smaller than the channel width aids controlling the size of the central fluid stream (cf. Figure 1a) (Anna et al. 2003, Garstecki et al. 2005, Ward et al. 2005). By changing the flow rate of Fluid 2 relative to Fluid 1 (cf. Figure 1c), the portion of the cross-section of the outlet channel occupied by Fluid 1 varies, and the size and shape of the central fluid stream in the outlet channel (referred throughout this work as the central focused stream) can thus be modified (Lee et al. 2006, Oliveira et al. 2011, Golden et al. 2012) . Throughout this work we will refer to the ratio between the inlet velocities (or flow rates - equivalent only if the cross-sectional areas of all inlets are the same as is the case in the present work) as the velocity ratio, $VR = U_2/U_1$, as defined in Figure 1c.

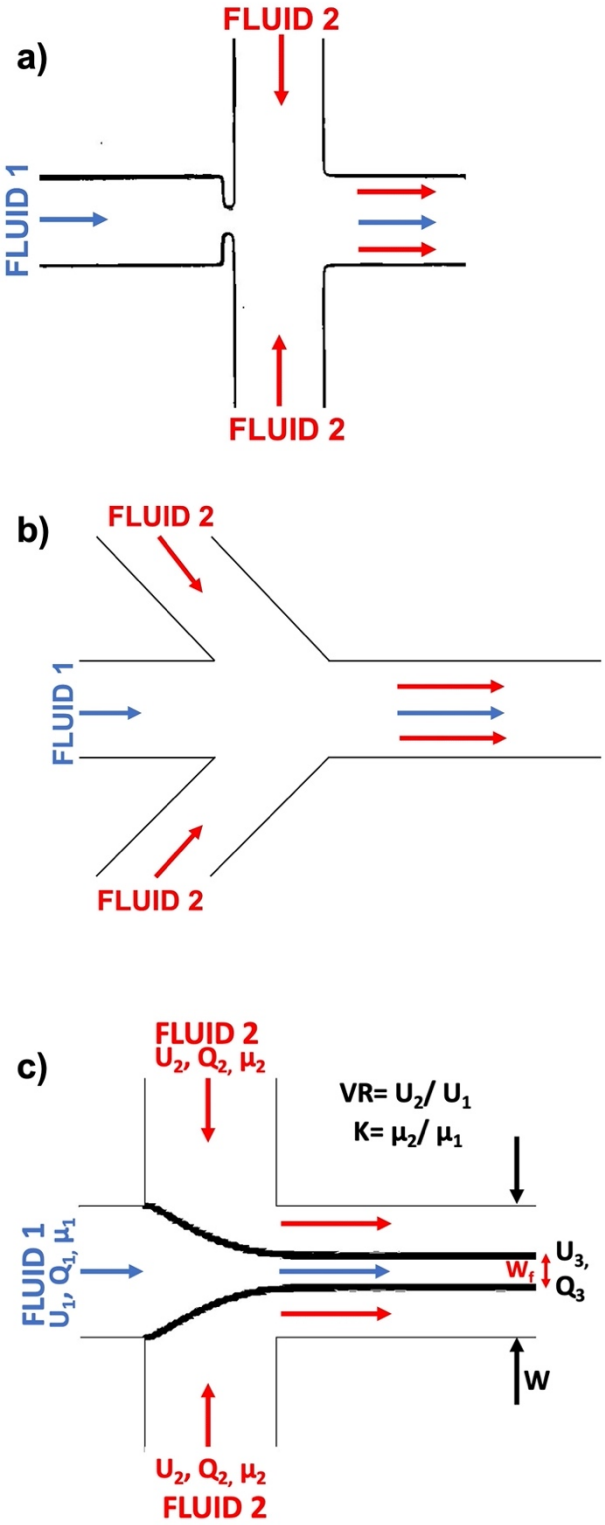

FIG 1. Examples of various flow focusing configurations used for bringing fluid streams into contact: a) where an orifice at the centre of the geometry is used to aid control of the shape of the outlet central focused stream; b) with angled lateral inlet streams, and c) with perpendicular lateral inlet streams. The latter configuration is used in this work and important variables are identified in the schematic, where μ_i, Q_i and U_i indicate the viscosity, flow rate and velocity of

each of the fluid streams, respectively. The subscripts i $=$ 1 and i $=$ 2 refer to the fluid in the central and lateral inlets, respectively.

The flow of different Newtonian fluid pairs, both miscible and immiscible, have been considered experimentally and numerically within microfluidic flow focusing devices (Knight et al. 1998, Lee et al. 2006, Hu and Cubaud 2016), highlighting the various parameters that affect the shape and size of the produced central focused stream. An early study by Knight et al (1998), showed that within channels of rectangular cross section (with aspect ratio defined as $AR = D/W$, where D refers to the depth of the channel), when using the same fluid in all inlets (arguably the most common case considered in the literature), the produced central focused stream at the outlet also exhibits an approximately rectangular cross section. This central focused stream is known to have a width that depends on the ratio of the inlet velocities, with this width decreasing significantly as $VR > 1$ (Knight et al. 1998, Lee et al. 2001, Lee et al. 2006, Oliveira et al. 2012). The ratio of viscosities of the inlet fluids ($K = {\mu_2}/{\mu_1}$) is another parameter that plays a crucial role in the formation and characteristics of the central focused fluid stream in microfluidic flow focusing devices. It is important to distinguish the different flow patterns that can be observed depending on the arrangement and characteristics of the fluids. For both miscible and immiscible fluid pairs, when the fluid in the central stream (of viscosity μ_1) is significantly more viscous than the fluid in the laterally injected streams (of viscosity μ_2), so that the ratio between the viscosities is smaller than 0.06, a cylindrical thread is formed (Cubaud and Mason 2012). This is usually referred to as a "lubricated viscous thread" or "core-annular flow" (Cubaud et al. 2012, Cubaud and Mason 2012, Cubaud 2020). Under these flow conditions the thread diameter has been found to be independent of the viscosity ratio, provided the abovementioned conditions are met (Cubaud and Mason 2006, Cubaud 2020). In contrast, when the central fluid is less viscous than the laterally injected fluid streams i.e. $K > 1$, fluid stratification occurs where each fluid, occupies a layer that spans the whole depth of the outlet channel from the top to the bottom channel walls. This yields an interfacial curvature between streams across the channel cross-section (Cubaud and Mason 2008, Cubaud and Mason 2012), with larger portions of the regions of high shear being occupied by the lower viscosity fluid (cf. Figure 2) where we show an example of

the cross-sectional shape of the central focused stream in the outlet channel obtained in our numerical simulations).

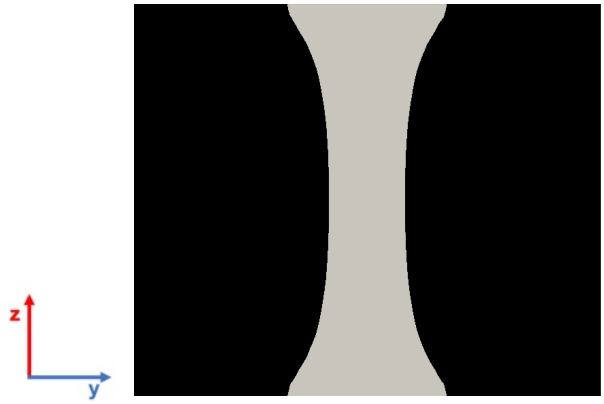

FIG 2. Example of the cross-sectional shape of the central focused stream in the outlet channel obtained in our numerical simulations for viscosity ratio $K > 1$ ($VR = 1, K = 9.56$) and $AR = 0.84$, where Fluid 1 is shown in grey and Fluid 2 is shown in black.

There have been a number of correlations proposed in previous research works to quantify the size of the central outlet focused stream, which have shown good agreement with experimental results under certain specific circumstances. In microfluidic devices (such as those considered in this work), the microchannels are typically planar with constant depth throughout, and a summary of proposed correlations for such channels is compiled in Table I. Please note that the list in Table I is not exhaustive, but we strive to provide relevant information about the fluid systems used and conditions under which each correlation applies.

TABLE I. Summary of previous studies, proposed correlations for estimating the size of the Newtonian fluid focused stream, and conditions under which they apply. For variable definitions see Figure 1.

Reference	Analytical Expression	Fluid Information	Experimental (Exp)/Numerical (Num)	Channel Cross-Section
(Knight et al. 1998)	$\frac{W_f}{W} = B\frac{(1+2\sigma-2\sigma\varphi)}{(1+2\sigma\gamma\varphi)}$ *where σ and γ reflect geometrical parameters, B is a constant of order 1 dependent on channel geometry and φ is the ratio of inlet pressures* $= {P_2}/{P_1}$.	Viscosity-matching streams ($K = 1$)	Exp	**Rectangular:** Channel with changing Aspect Ratio: Side and outlet channels $AR = 1$ Central inlet channel tapers down to a nozzle of $AR = 5$
(Wu and Nguyen 2005)	$\frac{W_f}{W} = \frac{1}{1+2\,(VR)\,K} = [1+2\,(VR)\,K]^{-1}$	**Newtonian Miscible Fluids:** Small variation in viscosity ratios ($1/1.8 \le K \le 1.8$)	Exp/2D Num/ Analytical (Hele-Shaw Limit)	**Rectangular (Exp):** $AR = 0.06$
(Cubaud and Mason 2006)	$W_f \approx \left(\frac{1}{2\,VR}\right)^{0.6}$	**Newtonian Miscible Fluids**: Viscous fluid is fully surrounded by a less viscous fluid. Lubricated viscous thread. Low Viscosity Ratios ($0.001 < K < 0.06$)	Exp	**Square**: $AR = 1$
(Lee et al. 2006)	$\frac{W_f}{W} = \frac{Q_1}{\gamma(Q_1+2Q_2)} = \gamma\,(1+2\,VR)$ $\gamma = \frac{\bar{v}_f}{\bar{v}_o} = \frac{1-\left({192D}/{\pi^5 W_f}\right)\sum_{n=0}^{\infty}\frac{1}{(2n+1)^5}\,\frac{sinh[(2n+1)\,\pi W_f/2D]}{cosh[(2n+1)\,\pi W/2D]}}{1-\left({192D}/{\pi^5 W}\right)\sum_{n=0}^{\infty}\frac{tanh[(2n+1)\,\pi W/2D]}{(2n+1)^5}}$ *where $\bar{v}_f$ and $\bar{v}_o$ represent the average velocities in the focused stream and outlet channel respectively.*	**Newtonian Miscible Fluids:** Viscosity-matching streams ($K = 1$)	Exp/ Analytical	**Rectangular:** $0.05 < AR < 1.78$
(Cubaud and Mason 2008)	$\frac{W_f}{W} \approx \left(\frac{Q_1}{2Q_2}\right)^{1/2} = \left(\frac{1}{2\,VR}\right)^{1/2}$	**Newtonian Immiscible Fluids**: Viscous fluid is fully surrounded by a less viscous fluid. Lubricated viscous thread. Low Viscosity Ratios ($0.0007 \le K \le 0.04$)	Exp	**Square:** $AR = 1$

(Cubaud and Mason 2008, Cubaud and Mason 2012)	$\frac{W_f}{W} \approx [1 + 2\,(VR)\,K]^{-1}$	**Newtonian Miscible:** High viscosity fluid surrounded by less viscous fluid: low viscosity ratios ($K = 0.002, 0.008, 0.016$) Low viscosity fluid surrounded by more viscous fluid: range of viscosity ratios ($K = 1.7, 6.3, 83, 625$)	Exp	**Rectangular:** $AR = 0.05$
(Cubaud et al. 2012, Cubaud and Mason 2012)	$\frac{W_f}{W} \approx \left[1 + 2\,(VR)\,K^{1/2}\right]^{-1}$	**Newtonian Miscible Fluids**: Low viscosity fluid surrounded by more viscous fluid. Large Viscosity Ratios ($K > 10$)	Exp	**Square**: $AR = 1$
(Hu and Cubaud 2016)	$\frac{W_f}{W} \approx \frac{1}{1 + 0.67\,(2\,VR)^{2/3}(K)^{1/2}}$ $\left(for\ \frac{W_f}{W} > 10^{-2}\right)$	**Newtonian Miscible Fluids:** Low viscosity fluid surrounded by more viscous fluid. Large viscosity contrasts ($100 \leq K \leq 10000$)	Exp	**Square**: $AR = 1$
(Cubaud 2020)	$\frac{W_f}{W} \approx \left(\frac{1/2VR}{2 + (1/2VR)}\right)^{1/2}$ Small flow rate ratios: $\frac{W_f}{W} \approx \left(\frac{1}{VR}\right)^{1/2}$	**Newtonian Miscible and Partially Miscible Fluids**: Viscous fluid fully surrounded by less viscous fluid. Lubricated viscous thread. Low Viscosity Ratios ($K \leq 0.1$)	Exp	**Square**: $AR = 1$

As illustrated in Table I, past research focuses mainly on conditions of either high viscosity ratios, low viscosity ratios or cases where the viscosity ratio is equal to 1. To date, studies, which cover a range of intermediate viscosity ratios, where differences have a large impact on the development of the central fluid focused stream, are limited.

In this paper, we report experimental and numerical simulations of miscible Newtonian fluid flows in microfluidic flow focusing devices to study in detail the combined effect of the viscosity ratio (for a range of intermediate K: $1 \leq K \leq 15.07$), the velocity ratio ($1 < VR < 20$) and geometrical aspect ratio on the characteristics of the central focused stream in the outlet channel. This work focuses on flows where every fluid stream remains in contact with the top and bottom channel walls and we report results that provide further insight into the curved interface that has been observed along the depth of the cross-section when high viscosity contrasts are present in parallel flow systems (Knight et al. 1998, Cubaud and Mason 2008, Cubaud et al. 2012, Cubaud and Mason 2012). We also present a 2D analytical expression derived from first principles for scaling the findings.

II. EXPERIMENTAL METHODOLOGY

The flow focusing configuration considered here is composed of four identical planar orthogonal channels (cf. Figure 3a) with two opposing lateral streams that shape a third central inlet stream. The reference fluid (Fluid 1), which is characterised by a dynamic viscosity μ_1, is inserted into the central inlet channel with a volumetric flow rate Q_1. Two additional fluid streams (Fluid 2, with a dynamic viscosity μ_2), are symmetrically injected into each of the lateral fluid inlets with a volumetric flow rate Q_2. The flow rates of the two opposing lateral streams are always kept equal to each other ensuring symmetric inlet flow conditions. In this case, the total flow rate in the outlet flow stream can be calculated as: $Q_3 = Q_1 + 2Q_2$. The corresponding average velocity in each of the streams can be calculated as $U_i = \frac{Q_i}{D_i W_i}$, where i represents either the core, lateral or outlet fluid streams ($i = 1, 2$ or 3, respectively). It is worth noting that in this type of device, the extensional rate can be varied by varying, for instance, the ratio between the flow rates in the lateral inlet streams and the central inlet stream (Oliveira et al. 2007, Sousa et al. 2009).

All microchannels were fabricated using polydimethylsiloxane (PDMS; Sylgard 184, Dow Corning) with a SU-8 mould using standard soft-lithography techniques. Subsequently, the microchannels were bonded to a PDMS coated glass slide to ensure that all surfaces had similar characteristics. A schematic diagram of the microfluidic geometry and the experimental set up are shown in Figure 3. The microfluidic flow focusing devices used exhibit a rectangular cross section of width, $W = 109 \pm 2\ \mu m$ and a uniform depth, $D = 92 \pm 1\ \mu m$, which results in an aspect ratio, defined as the ratio of the channel depth to the channel width ($AR = D/W$) that is constant throughout the device and equal to 0.84. To analyse the effect of the channel aspect ratio, an additional geometry having width $W = 125 \pm 2\ \mu m$ and depth $D = 27 \pm 1\ \mu m$ (aspect ratio of $AR = 0.22$) was also used.

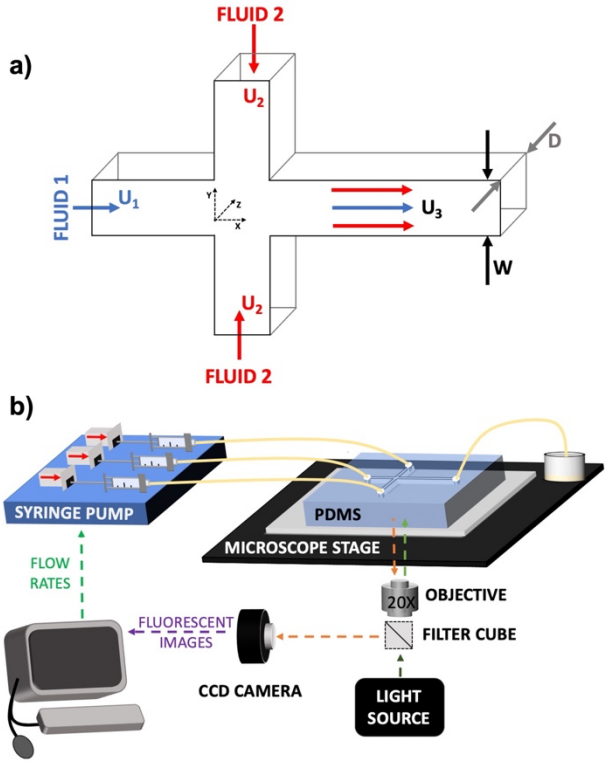

FIG 3. Schematic of a) 3D Microfluidic flow focusing device used in this work showing relevant variables and coordinate system, and b) experimental flow visualisation set up.

To study the effect of viscosity ratio, aqueous solutions of glycerol of varying concentrations were prepared. The solutions were then divided into three samples for flow visualisation purposes: sample (A), in which Rhodamine-B dye (Sigma-Aldrich) at a concentration of approximately 0.016% was added; sample (B), in which fluorescent tracer particles with nominal diameter of 1μm (FluoSpheres carboxylate-modified,Nile Red (Ex/Em: 535/575)) were added at concentration of approximately 0.02%wt; and sample (C) which was left as the original solution. A summary of the composition and properties of these fluids is given in Table II, with GLY52 being used as the reference fluid. The density of the solutions was measured using pycnometry and the viscosity was characterised in steady shear on a DHR-2 hybrid rotational rheometer (TA Instruments) with a cone-plate geometry (60 mm diameter, 1° cone angle) at a temperature of 20°C.

TABLE II. Characteristics of the fluids used in the experimental work including fluid composition and physical properties (density and viscosity) at 20 °C.

Fluid ID	Composition	Density (kg/m^3)	Viscosity (Pa s)	Viscosity Ratio (K)*
Water	Deionised Water	1000	$1.00x10^{-3}$	0.15
GLY52	***51.7 % Glycerol**	**1172**	**$6.81x10^{-3}$**	**1**
GLY61	61.4 wt% Glycerol	1181	$1.20x10^{-2}$	1.76
GLY71	71.2 wt% Glycerol	1190	$2.55x10^{-2}$	3.74
GLY76	75.6 wt% Glycerol	1195	$3.84x10^{-2}$	5.64
GLY81	80.5 wt% Glycerol	1209	$6.51x10^{-2}$	9.56
GLY84	84.4 wt% Glycerol	1222	$1.03x10^{-2}$	15.07

*Viscosity ratio calculated relative to GLY52 used as reference fluid.

The fluids were injected into the three geometry inlets simultaneously at controlled flowrates using a high-precision syringe pump with independent modules (neMESYS, Cetoni GmbH). SGE™ gastight glass syringes were connected to the microchannel using Tygon tubing, and the geometry outlet was left open to the atmosphere. The flow was illuminated with a 100W metal halide lamp and visualised using an inverted microscope (Olympus IX71). The microscope was equipped with a 20X objective lens (numerical aperture NA = 0.4) and an adequate filter cube (Olympus U-MWIGA3). The images were acquired at the centre plane of the microchannel ($z = D/2$), unless stated otherwise, using a CCD camera (Olympus XM10) and the exposure time was adjusted according to the flow conditions.

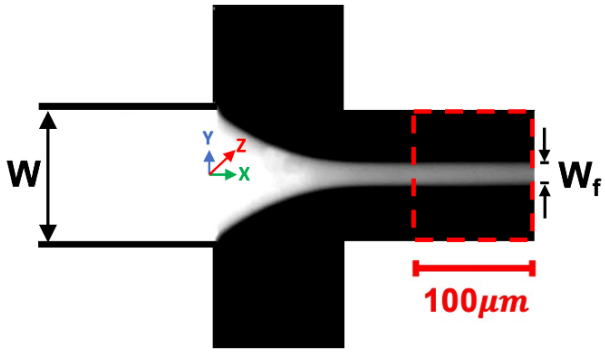

FIG 4. Example of a microscope image obtained with the central fluid stream dyed with Rhodamine-B and undyed lateral streams, highlighting the region over which the measurement of the outlet central focused stream width was performed (the reported value of W_f being an average across the highlighted region).

We used image analysis to assess the impact of viscosity ratio, velocity ratio and aspect ratio of the device on the shape and size of the generated central fluid focused stream. The width of the central focused stream in the outlet channel at the centre plane, W_f, was measured using the image processing software ImageJ in the region of the bounding rectangle indicated by the red box in Figure 4. The bounding measurement rectangle spanned ~100μm along the x-direction in the region of $1.7 \leq x/W \leq 2.7$ where the newly formed central focused stream exhibited an approximately constant shape. An average value for the focused stream width over this length was then determined. It is important to note that defining the exact boundaries for these measurements is not straightforward due to a small gradient in the interface region between the two fluids as illustrated by the gradual variation of grayscale intensity profile shown in Figure 5. For consistency, the mid-point was considered for the measurements presented in this work.

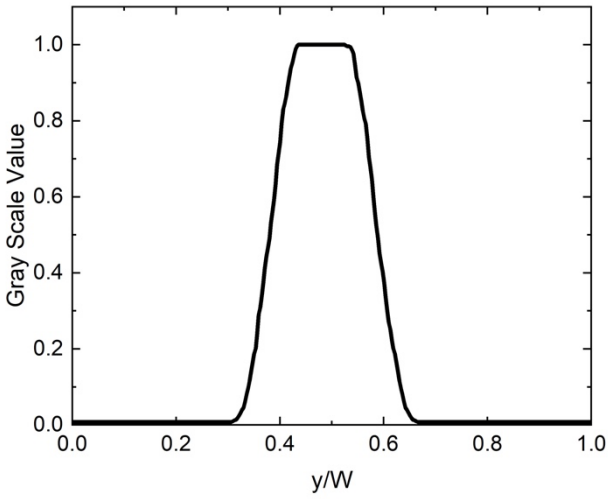

FIG 5. Normalised grayscale profile along the width of the outlet channel at location $\frac{x}{W} = 2.5$ (within the experimental measurement region) for $AR = 0.84$, $K = 1$ and $VR = 1$. The profile highlights the variation of grayscale intensity in the regions of the interface between the undyed outer fluid and the central focused fluid stream dyed with Rhodamine-B.

For all 3D simulations, measurements were taken at a location in the downstream channel, corresponding to $x/W = 2.5$. This location lies within the experimental measuring window to ensure comparable results. This measurement location is also comparable to that used in the work of Cubaud et al (2008) ensuring the flow is fully developed in the outlet stream without being too far downstream thus avoiding significant diffusion effects, as witnessed by Wu et al (2005).

III. DIMENSIONLESS PARAMETERS

Dimensionless parameters of interest for the flow under consideration include the Reynolds number, Re, the viscosity ratio, $K = \mu_2/\mu_1$, and the velocity ratio, $VR = U_2/U_1$, which in our case is equal to the flow rate ratio Q_2/Q_1, given the incompressibility constraint and to the fact that the inlet channels have the same cross-sectional area. Given the significant role played by the velocity ratio on the characteristics of the central outlet stream, the effect of this parameter was systematically investigated throughout this work. To this end, the central flow rate was maintained constant throughout the whole set of experiments, while the flow rate of the lateral streams was systematically

increased. When the fluid is the same in all inlet streams ($K = 1$), for low values of VR (i.e., for $VR < 1$) the central stream encompasses a large portion of the outlet channel, leaving only a thin region for the flow of the outer fluid streams (Hu and Cubaud 2016). In this work, however, we focus on larger values of VR (i.e., $VR \geq 1$), for which, as we shall see, a relatively narrow central focused stream is observed. Inertial effects are not important since the Reynolds numbers considered here are small ($0.01 < Re < 0.5$).

IV. NUMERICAL METHOD

In addition to experiments, a set of selected three-dimensional simulations were carried out using a Volume-of-Fluid (VOF) method using the opensource computational toolbox OpenFOAM. In such an approach, the interface between the fluids is described through the adoption of a volume fraction phase, α. This represents the volume average of one fluid (arbitrarily defined between two possible choices) with respect to the total fluid encapsulated in one computational cell. Thus, this function takes values $0 < \alpha < 1$ at the interface, while the values 0 and 1 characterise the two bulk phases away from the interface. Such quantity is then evolved numerically in space and time through an advection equation of the type reported below (albeit particular modifications required to avoid excessive smearing of the interface introduced in the implementation of the method in OpenFOAM e.g., see (Capobianchi et al. 2017) for more details):

$$\frac{\partial \alpha}{\partial t} + \nabla \cdot (\mathbf{u}\alpha) = 0. \tag{1}$$

Finally, since we are considering miscible fluids, capillary forces are not taken into account, and the 'one-fluid' formulation of the momentum equation reads (note that gravity is not accounted for due to the small length scale and similar density of the two fluids):

$$\rho \left[\frac{\partial \mathbf{u}}{\partial t} + (\mathbf{u} \cdot \boldsymbol{\nabla})\mathbf{u} \right] = -\boldsymbol{\nabla} \mathrm{p} + \boldsymbol{\nabla} \cdot (2\mu \mathbf{D}), \tag{2}$$

where $\mathbf{D} = \frac{\mathbf{1}}{\mathbf{2}}(\boldsymbol{\nabla}\mathbf{u} + (\boldsymbol{\nabla}\mathbf{u})^{\mathrm{T}})$ is the rate-of-strain tensor. In such an approach, variables, i.e., velocity and pressure, are defined continuously throughout the whole domain, while the fluid properties are continuous functions of the volume fraction:

$$\rho = \alpha\rho_1 + (1-\alpha)\rho_2, \qquad \mu = \alpha\mu_1 + (1-\alpha)\mu_2. \tag{3}$$

The problem was discretised numerically using a structured mesh consisting of approximately 3×10^5 identical cubic cells and an adaptive octree mesh refinement approach has been applied at the region of the interface (only for the 3D cases), where larger resolution was deemed necessary. It should be noted that the thickness of the central stream undergoes substantial variations depending on the flow conditions considered (i.e., velocity ratio and/or viscosity ratio), hence the level of refinement adopted was selected on the basis of this constraint. In other terms, since the density of the unrefined mesh was always the same, the dimension of the cells to be employed at the interface was necessarily different for different flow conditions across the whole region of the flow parameter explored to have a sufficiently high resolution.

V. ANALYTICAL SOLUTION FOR THE TWO-DIMENSIONAL PROBLEM

In this section, an exact solution for the two-dimensional creeping flow, obtained assuming absence of confinement in the spanwise z-direction, is derived by taking advantage of the symmetry of the flow established at a sufficient distance downstream of the cross junction. Owing to these hypotheses, the problem can be simplified to that of a pressure-driven, creeping flow between 2 parallel plates (cf. Figure 6) in which the interface between the fluids is perfectly flat. A schematic of the problem highlighting the coordinate system adopted, and the equivalent symmetric counterpart of the flow is shown in Figure 6.

The problem under consideration is governed by the steady-state Navier-Stokes equations for incompressible creeping flows for the two fluids considered:

$$0 = -\frac{\partial p}{\partial x} + \mu_1 \frac{\partial^2}{\partial y^2}(u_{1,x}), \tag{4}$$

$$0 = -\frac{\partial p}{\partial x} + \mu_2 \frac{\partial^2}{\partial y^2}(u_{2,x}), \tag{5}$$

where $u_{1,x}$ and $u_{2,x}$ are the x-component of the velocities of Fluid 1 and Fluid 2, respectively. The origin of the y-axis is taken at the centreline (dashed line in Figure 6). The central stream is characterised by a half height $h = W_f/2$, while $H = W/2$ represents the vertical extension of the semi portion of the domain.

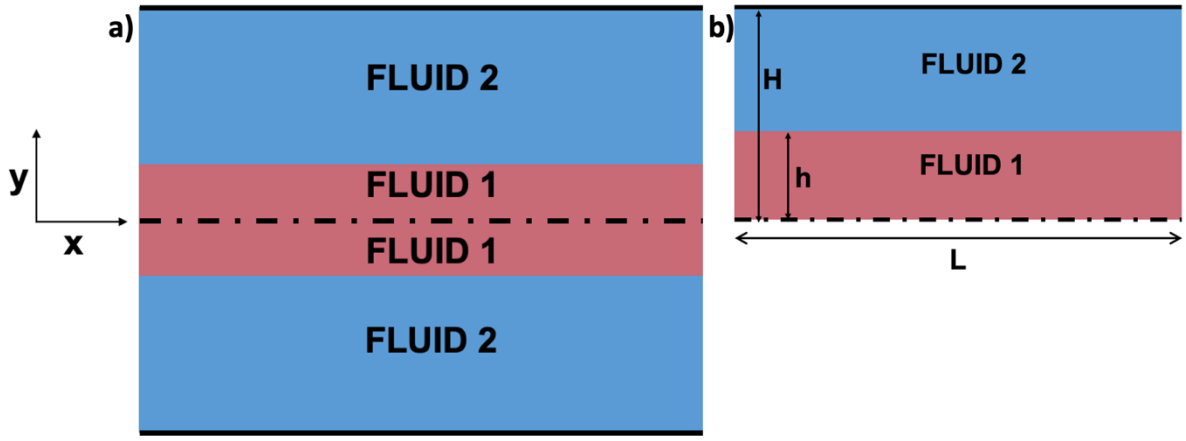

FIG 6. Schematic of a) the full 2D geometry used to replicate the outlet channel of the flow focusing device highlighting the region of symmetry and the employed coordinate system, b) the 2D geometry used to derive the 2D analytical expression considering the symmetry of the flow.

The general solutions of equations (4) and (5) are:

$$u_{1,x} = \frac{Gy^2}{2\mu_1} + Ay + B, \qquad u_{2,x} = \frac{Gy^2}{2\mu_2} + Cy + D, \tag{6}$$

where G is the applied constant pressure gradient defined as $G = \Delta p/L$, L is the length of the domain in the x-direction and A, B, C and D are yet to be determined constants of integration. Given the geometrical constraints of the flow and its boundary conditions, the y-component of the velocity is null everywhere, i.e., $u_{1,y} = u_{2,y} \equiv 0$. At the fluid interface ($y = h$), continuity of the velocity and of the shear stress is imposed, while at the upper wall ($y = H$), we impose the no-slip boundary condition, i.e.

$$u_{1,x}\big|_{y=h} = u_{2,x}\big|_{y=h} \tag{7}$$

$$\mu_1 \frac{\partial u_{1,x}}{\partial y}\bigg|_{y=h} = \mu_2 \frac{\partial u_{2,x}}{\partial y}\bigg|_{y=h} \tag{8}$$

$$u_{2,x}\big|_{y=H} = 0. \tag{9}$$

By substituting these boundary conditions into equation (6) we found the following expressions for each constant: $A = 0,\ B = \frac{-G\left(H^2\mu_1 - h^2\mu_1 + h^2\mu_2\right)}{2\mu_1\mu_2}$, $C = 0,\ D = -\frac{GH^2}{2\mu_2}$, which allows determining $u_{1,x}$ and $u_{2,x}$ as:

$$u_{1,x} = -\frac{G\left(\left(H^2 - h^2\right)\mu_1 + \mu_2\left(h^2 - y^2\right)\right)}{2\mu_1\mu_2}, \qquad u_{2,x} = -\frac{G\left(H^2 - y^2\right)}{2\mu_2}, \tag{10}$$

The average velocities of each fluid stream (i.e. $u_{1,x}$ and $u_{2,x}$) can then be calculated as follows:

$$U_{1,x} = \frac{1}{h}\int_0^h u_{1,x}dy = -\frac{\left((H^2 - h^2)\mu_1 + \frac{2h^3\mu_2}{3}\right)G}{2\mu_1\mu_2}, \tag{11}$$

$$U_{2,x} = \frac{1}{(H-h)}\int_h^H u_{2,x}dy = -\frac{(2H + h)\,G\,(H - h)}{6\mu_2}. \tag{12}$$

Substituting the following variables for the dimensionless focused stream width, $\delta = h/H$ and the viscosity ratio, $K = \mu_2/\mu_1$ into the previous equations, we obtain the following expression for the velocity ratio:

$$VR \equiv \frac{U_{2,x}}{U_{1,x}} = \frac{(\delta+2)(\delta-1)^2}{(4K-6)\delta^3 + 6\delta}. \tag{13}$$

For a desired value of the velocity ratio and viscosity ratio, it is therefore possible to determine the dimensionless thickness δ which satisfies equation (13).

VI. ANALYTICAL SOLUTION AND NUMERICAL RESULTS FOR THE 2D PROBLEM

The dimensionless width of the central focused stream (normalised using the channel width) in the fully developed region of the outlet channel of the flow focusing device obtained in the 2D flow numerical simulations is compared with the analytical 2D solution derived in Section V. A strong effect of the velocity ratio (especially for low VR values) on the width of the central focused stream is observed as seen in previous work (Wu and Nguyen 2005, Oliveira et al. 2012), with the width decreasing as VR is increased. The viscosity ratio is also seen to impact the size of the focused stream for $VR = 1$, however this effect is not as significant for higher values of K over the ranges considered. There is excellent quantitative agreement between the 2D numerical and analytical results for a range of VR (Figure 7a) and K values (Figure 7b) with a maximum relative error of 7%. It is worth noting that the relative errors are smaller for lower values of VR and K. The analytical solution also shows that for higher values of VR, the effect of K becomes less and less significant (for $VR = 5$ e.g., as shown in Figure 7b, the relative difference between the normalised width for $K = 1$ and $K = 15$ is $\lesssim 3\%$).

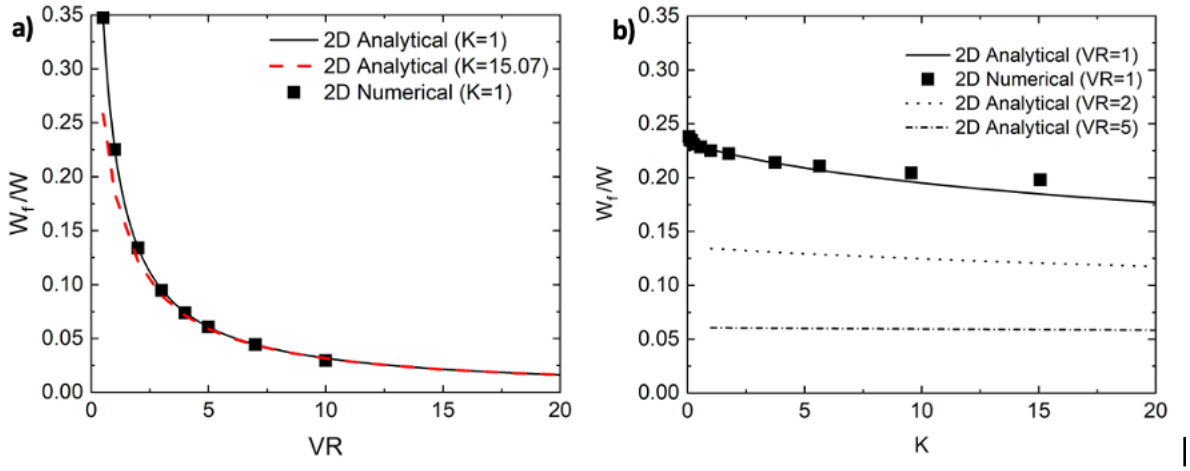

FIG 7. Comparison of 2D analytical solution and 2D numerical simulations (at $x/W = 2.5$) showing a) Impact of velocity ratio for $K = 1$ b) Impact of viscosity ratio for $VR = 1, VR = 2$ and $VR = 5$.

Good agreement between the 2D numerical and analytical results can also be observed in terms of velocity distribution in the cross section of the outlet channel (normalised using the maximum velocity at the centreline ($y/W = 0.5$) for each case) for a range of K values and $VR = 1$ (Figure 8). When $K = 1$ (Figure 8a), the velocity profile exhibits a symmetric parabolic shape across the width of the cross-section as expected. As K is increased beyond unity (Figure 8b-d), while the profiles remain symmetric, an additional central peak can be visualised, becoming more pronounced as K increases. For increasingly larger viscosity ratios, it can be noted in both Figure 7 and Figure 8 that the agreement becomes less accurate, which can be attributed to the numerical approach which considers the two fluids as a single entity characterised by generally different material properties, such as the viscosity, as appropriate in this context. Discontinuities in properties across the interface are linearised by means of equation (3). This, in turn, inevitably introduces inaccuracies in the numerical solution which become less reliable for increasingly large viscosity ratios: an issue, which could be partially mitigated by the adoption of larger mesh resolutions.

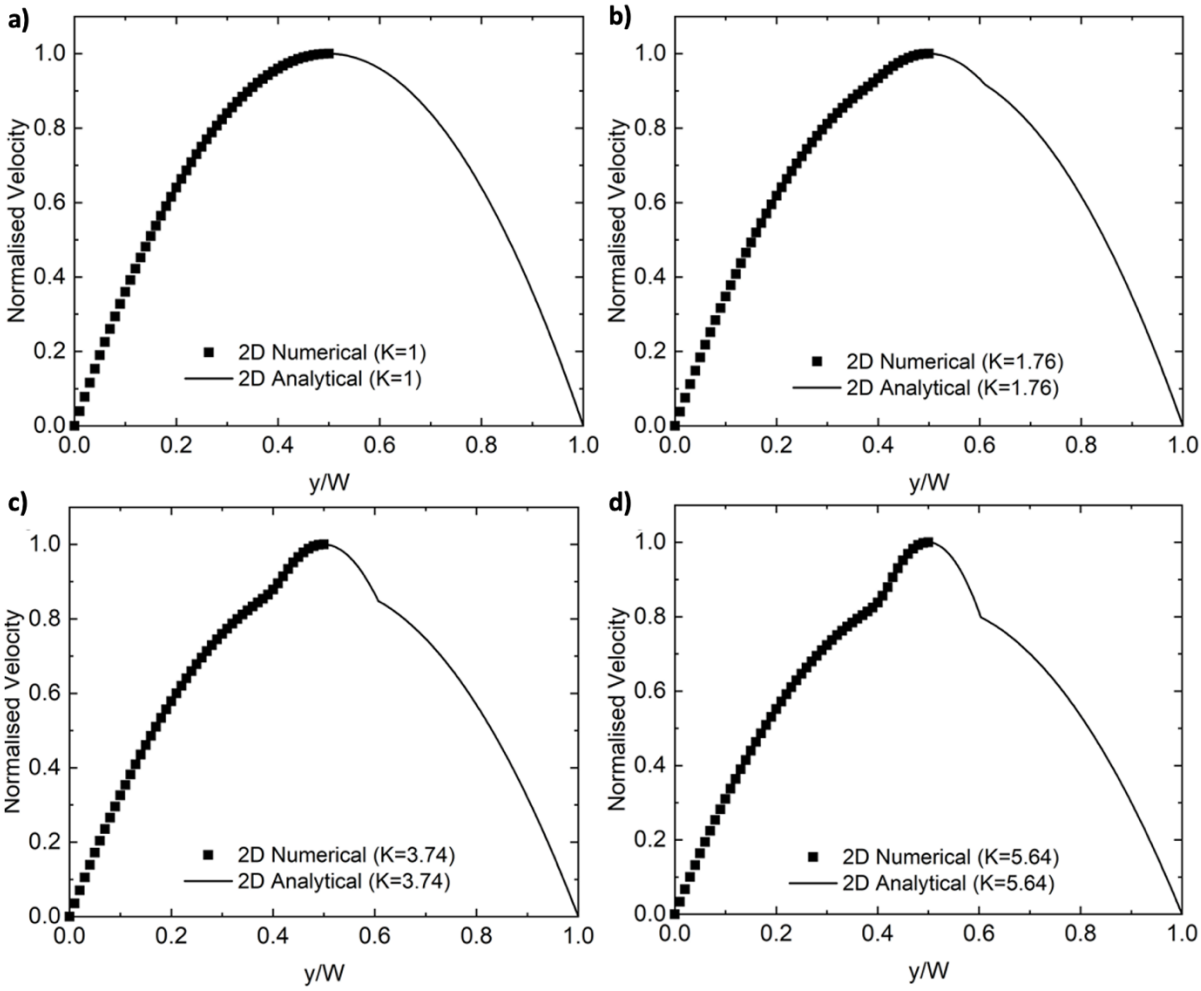

FIG 8. Comparison of 2D analytical solution and 2D numerical simulations (at $x/W = 2.5$) showing the impact of viscosity ratio when $VR = 1$ on the normalised velocity profile (normalised using the maximum velocity at the centreline ($y/W = 0.5$) for each case) in the y-direction for a) $K = 1$ b) $K = 1.76$ c) $K = 3.74$ and d) $K = 5.64$.

VII. RESULTS AND DISCUSSION

In this work, a series of experiments supported by 3D numerical simulations were conducted to investigate the influence of various parameters on the characteristics (shape and width) of the central focused outlet fluid stream. As anticipated, we focus on those conditions where inertia can be assumed negligible, and the flow is always steady and symmetric about the x-axis (Lee et al. 2006). We also neglect molecular diffusion as in most cases the Peclet number (defined as $Pe = U_3 W/D_c$, where D_c is the diffusion

coefficient for each fluid pair, as detailed by Petitjeans and Maxworthy (1996) is large ($Pe > 10^3$) suggesting the two miscible fluids flow side by side without mixing (Petitjeans and Maxworthy 1996, d'Olce et al. 2009). It is important to note that when interfacial tension is relatively low or miscible fluids are considered, the flow may experience an instability referred to as viscosity stratification (Yih 1967). To avoid such instabilities, previous researchers have reported that high values of interfacial tension can be used (Hooper and Boyd 2006) or, as this instability is said to be of inertial origin, low Reynolds number flows (Bonhomme et al. 2011). It is possible that our system may not be truly steady state; however, since for all cases considered here, the Reynolds number was always below unity and no visible instabilities were identified, in agreement with the results of Bonhomme et al. (2011), we will treat the system as being stable throughout this work (as done previously in Davoodi et al. 2021).

A. Effect of Velocity Ratio

To assess the impact of the velocity ratio, experiments were conducted considering viscosity matching streams (i.e., considering $K = 1$), in which the velocity ratio, VR, was adjusted from $VR = 1$ up to the maximum value of $VR = 20$. Simulations for some selected cases were also performed for comparison. Typical flow patterns encountered for the base case geometry ($AR = 0.84$) can be observed in Figure 9.

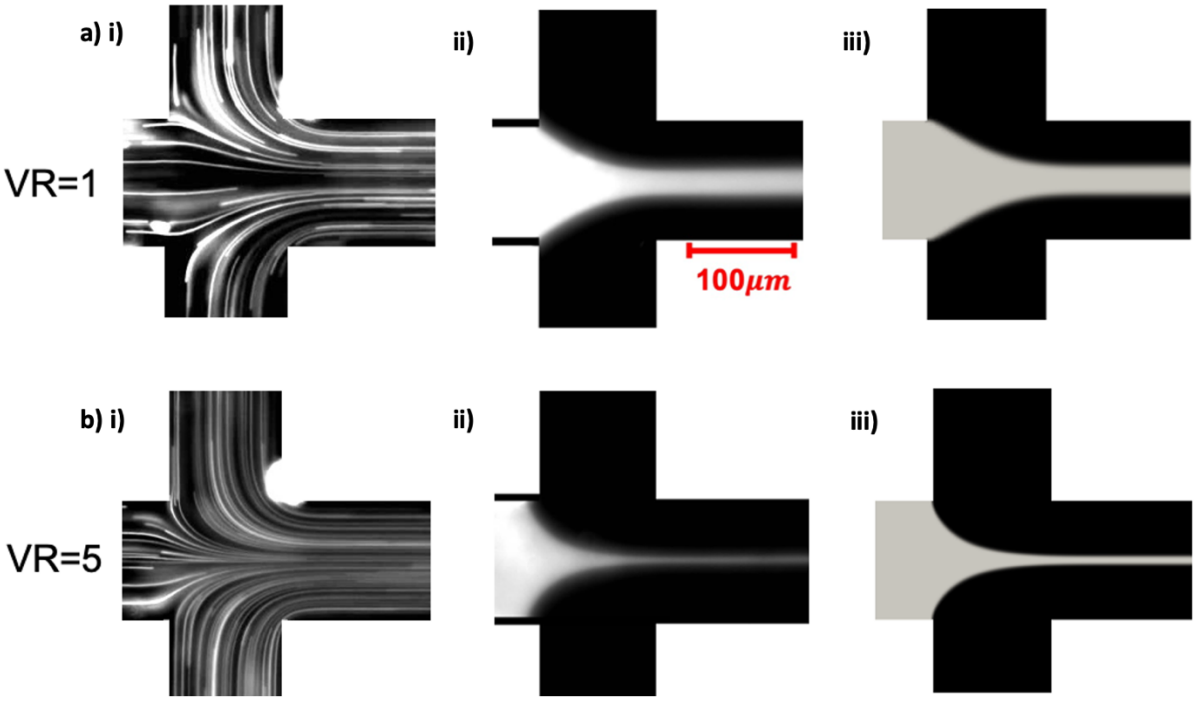

FIG 9. Flow patterns observed in the flow focusing geometry with $AR = 0.84$ and $Q_1 = 0.02$ ml/h, with matching fluid in all inlets ($K = 1$) and different velocity ratios a) $VR = 1$, b) $VR = 5$. i-ii) Experimental images obtained by adding i) fluorescent tracer particles to all inlet streams to show the pathlines and ii) Rhodamine-B dye to the central fluid inlet only. iii) 3D numerical simulations, where Fluid 1 is shown in gray and Fluid 2 is shown in black.

For the cases shown in Figure 9, a converging flow region is present at the centre of the flow focusing device, producing a centralised straight focused stream downstream of the central region that extends along the outlet of the microchannel. In agreement with previous works for $K = 1$ (e.g. Lee et al. 2006), the width of the central focused stream decreases as the velocity ratio is increased, and its cross sectional area is approximately rectangular (Knight et al. 1998). For all VR tested here ($1 < VR < 20$), the separating streamlines in the central region of the device where the three inlet fluids meet display a concave shape (as seen in the experimental flow patterns of Figure 9ai and bi, and in the numerical results shown in Figure 10) as expected when $VR > K^{-3/4}/2$ (Hu and Cubaud 2016). The streamlines in the converging region near the centre of the geometry (c.f. Figure 9) exhibit a near hyperbolic shape characteristic of extensional flows (Oliveira et al. 2007). Increasing VR to higher values, increases the curvature of the streamlines and reduces the width of the central outlet focused stream (Nguyen and Huang 2005, Oliveira

et al. 2012). Under these conditions the viscous stresses from the lateral fluid streams dominate how the central fluid profile is formed. Similar experimental observations are discussed in the work of Lee et al (2006) where the range of $0.1 \leq VR \leq 8$ was studied for $K = 1$.

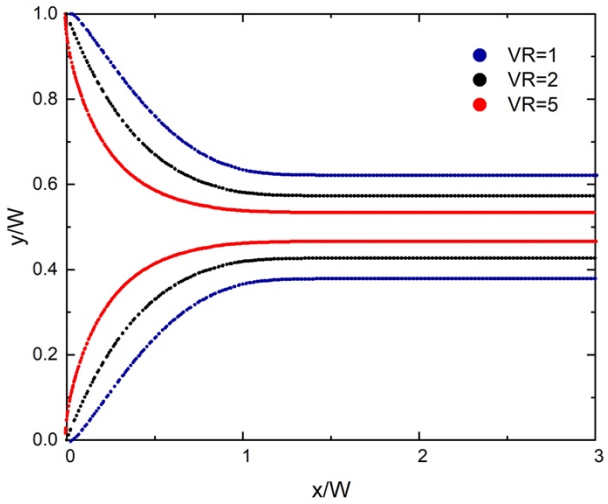

FIG 10. Outline of the separating streamlines observed from numerical simulations at the centre plane with increasing velocity ratio within the flow focusing geometry of $AR = 0.84$, for $K = 1$.

The size of the central focused stream developed in the outlet channel is quantified in Figure 11, where the measured central focused stream thickness measured experimentally at the centre plane is normalised using the channel width. In this figure, results predicted by the simulations and by the analytical solution (Equation (13)) are also included.

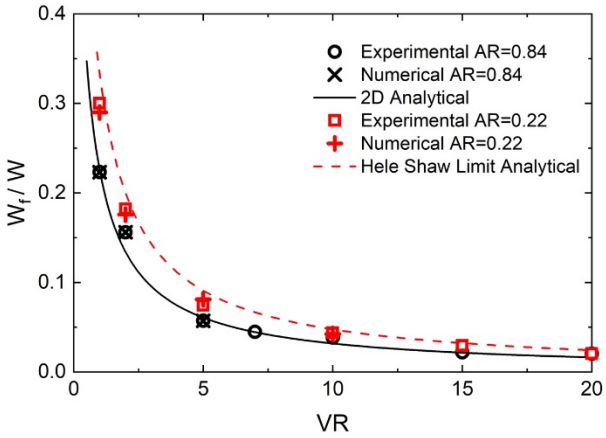

FIG 11. Experimental measurements and 3D numerical simulation results of the normalised width of the central focused outlet stream at the centre plane of the flow focusing geometries of $AR = 0.84$ and $AR = 0.22$ with increasing velocity ratio for $K = 1$. Comparison of the results with the derived 2D analytical solution (Equation (13)) and Hele-Shaw solution $\frac{W_f}{W} = [1 + 2\,(VR)K]^{-1}$ (Wu and Nguyen 2005) are also shown.

The experimental and 3D numerical results show an excellent agreement. The two-dimensional analytical solution also captures well the experimental and numerical results in the channel with $AR = 0.84$, showing the ability of the two-dimensional analytical solution to capture reasonably well the dynamics of the focused stream in these particular conditions. In addition to the base case of $AR = 0.84$, we also show in the figure the case of $AR = 0.22$. Again, there is an excellent agreement between experimental measurements and 3D numerical simulations. However, as expected in this case, deviations from the analytical solution are observed, which can be attributed to the fact that, as the microchannel becomes shallower, the 2D approximation becomes less accurate and the experimental values are better captured by the analytical solution proposed by Wu and Nguyen (Wu and Nguyen, 2005) in the Hele-Shaw limit.

B. Effect of Viscosity Ratio

The effect of the viscosity ratio, K, was analysed experimentally by increasing the glycerol concentration in the two lateral inlet streams, while maintaining the same reference fluid in the central inlet stream. Numerical simulations were also performed for comparison and to provide additional insight that would be challenging to obtain experimentally (e.g.,

the detailed shape of the interface along the depth direction). As shown qualitatively in Figure 12, for $VR = 1$, the viscosity ratio is seen to have a small effect on streamline curvature in the central region of the device where the inlet streams meet (particularly for low values of K), and strongly impacts the shape/curvature of the interface along the depth of the microchannel cross section, i.e. along the z-direction.

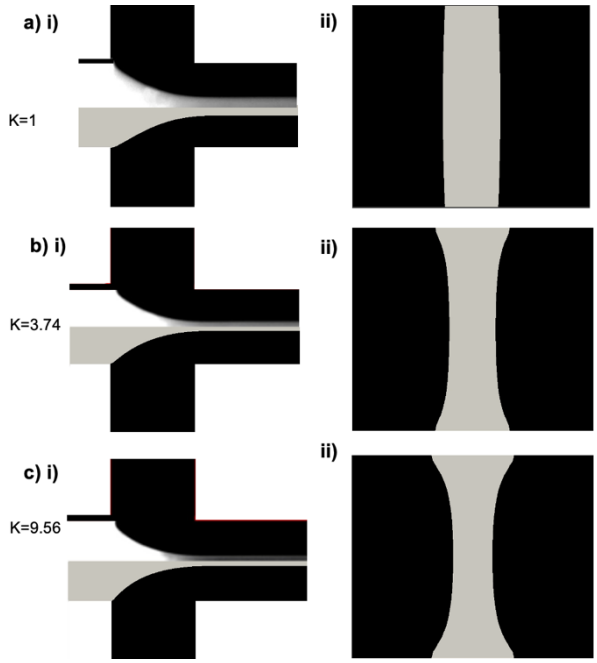

FIG 12. Qualitative flow patterns observed in the flow focusing geometry with $AR = 0.84$, for $VR = 1$ and three viscosity ratios a) $K = 1$, b) $K = 3.74$, and c) $K = 9.56$: i) comparison of experimental (top half) and 3D numerical simulation (bottom half) at the $z = D/2$ centre plane, showing the focusing of the central stream ; ii) 3D numerical simulations showing the filament cross-section in the y-z plane at $x/W = 2.5$, where Fluid 1 is shown in grey and Fluid 2 is shown in black.

Similarly to the effect of velocity ratio, the normalised central focused stream width at the $z = D/2$ centre plane was found to decrease in size as the viscosities of the lateral fluids increased relative to the viscosity of Fluid 1. Good agreement was found between the dimensionless focused stream size obtained in the experiments and in our 3D numerical simulations for $AR = 0.84$. (c.f. Figure 13).

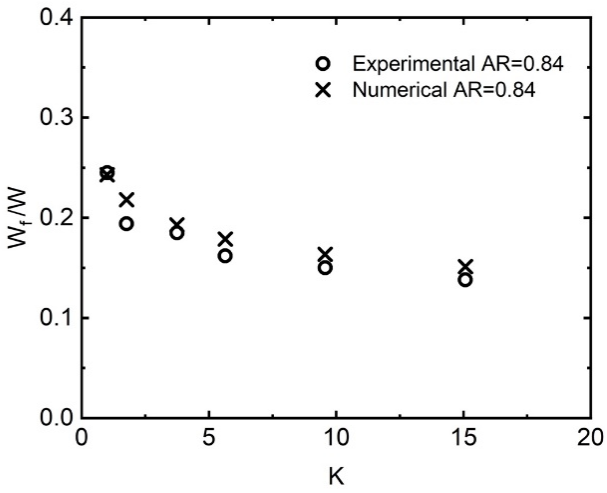

FIG 13. Impact of viscosity ratio on the normalised width of the central focused outlet stream at the $z = D/2$ centre plane for $VR = 1$. Comparison of experimental and 3D numerical simulations for $AR = 0.84$.

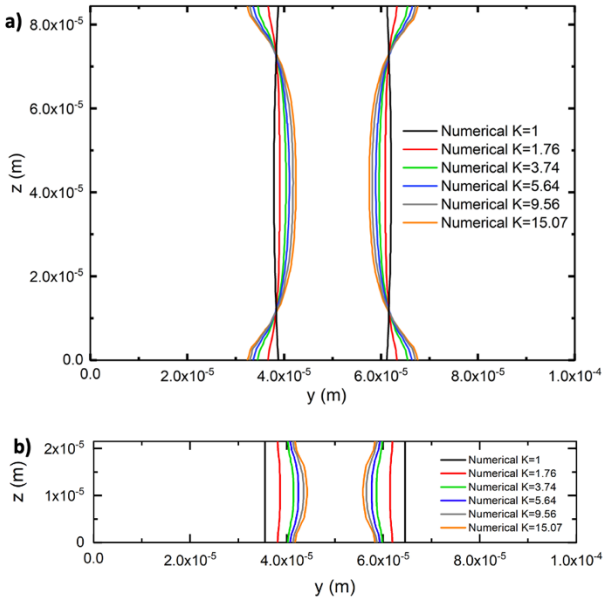

FIG 14. Variation of the cross-sectional shape of the central focused stream with viscosity ratio for $VR = 1$. Comparison of the profile of the interface along the channel depth with increasing K obtained using 3D numerical simulations with a) $AR = 0.84$, and b) $AR = 0.22$.

When the two fluids have the same viscosity ($K = 1$), the central focused stream in the outlet channel exhibits an approximately rectangular cross-section (cf. Figure 12aii), as also reported in the work of Knight et al (1998). When $K > 1$, the interface location varies along the depth of the cross section (Figure 12bii and cii), showing a concave shape,

where the central focused stream width is larger at the walls than at the centre plane of the microchannel ($z = D/2$), where our experimental measurements of the central focused stream size are typically taken. Similar effects have also been observed in other type of geometries, such as the microfluidic cross slot (Davoodi et al. 2021) and in the T-channels (Guillot et al. 2006); as well as in flow focusing configurations similar to those considered here (Guillot et al. 2006, Cubaud and Mason 2012, Hu and Cubaud 2016), however these studies have not shown how the shape changes with the ratio of inlet viscosities. For parallel flows, when large viscosity ratios are considered, the less viscous fluids are known to migrate towards the regions of high shear near the channel walls while the more viscous fluids move to the regions of low shear (Joseph et al. 1984). This interfacial curvature is therefore deemed to be a "self-lubricating" aspect of the flow (Cubaud and Mason 2008).

Figure 14 shows the shape of the central focused stream cross-section obtained numerically for a wide range of values of K for $AR = 0.84$ (Figure 14a) and $AR = 0.22$ (Figure 14b). It can be observed that as K increases beyond unity, the shape of the focused stream interface moves away from the case of a nearly straight interface seen when all fluid streams have the same viscosity. The difference between the central focused stream width at the channel walls and the minimum width at the centre plane of the microchannel becomes larger as the lateral streams become more viscous than the central stream.

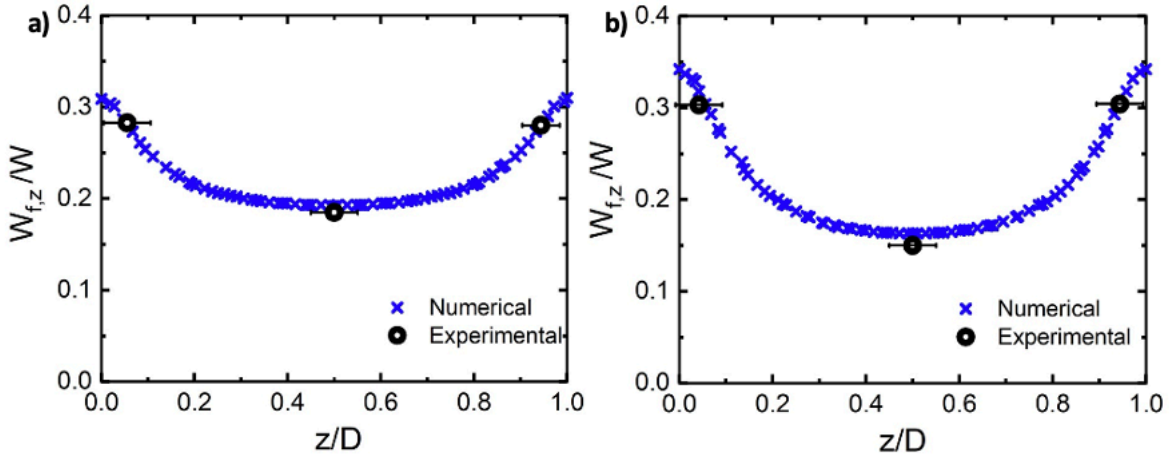

FIG 15. Comparison of the normalised width of the central focused outlet stream along the z-direction obtained in the 3D numerical simulations and in the experiments with $AR = 0.84$ for a) $K = 3.74$, and b) $K = 9.56$. $W_{f,z}$ represents the filament width at a particular z position ($0 < z/D < 1$) and horizontal error bars indicate the experimental depth of field estimated for our optical set-up.

Figure 15a and b show a quantitative comparison between experimental and numerical results of the width of the central focused stream along the depth of the channel for two viscosity ratios ($K = 3.74$ and $K = 9.56$). Although experimental measurements could not be taken accurately over the full length of the channel using our approach, we are able to perform measurements in three specific locations: close to each of the channel walls and the centre of the cross section (i.e. for $z = D/2$). Good agreement was found between experiments and numerical simulations for all viscosity ratios studied, showing the good accuracy of the numerical framework (it should be noted that only a selection of results is displayed here for the sake of conciseness).

Contours of the shear component of the rate-of-strain tensor, S_{xy}, and its magnitude, $S = \sqrt{\boldsymbol{S}:\boldsymbol{S}}$, taken for a cross-section in the y-z plane at $x/W = 2.5$ (location in the outlet channel away from the junction), and normalised with a reference stress ($\mu_1 U_3/W$ where μ_1, U_3 and W are defined in Section II), are shown in Figure 16 for three different values of the viscosity ratio: $K = 1, 3.74, 9.56$. Lines showing the location of the interface are superimposed on each image. Not surprisingly, for $K = 1$, S is distributed almost

symmetrically, since the two fluids have the same viscosity, thus corresponding to the stress field obtained in a single fluid configuration. Nevertheless, with reference to Figure 16a, due to the fact that the cross-section is characterised by an aspect ratio different from unity ($AR = 0.84$), stresses generated at the walls propagate over different lengths along the two coordinate directions resulting in a slightly curved interface. As the viscosity of the lateral channels' fluid is increased ($K > 1$), in addition to the geometrical constraint mentioned above, the stress field is also influenced by the presence of the interface, where the stresses experience a discontinuity since here $(S_n)_1/(S_n)_2 = K$, where $S_n = S_{xy}n_y + S_{xz}n_z$ is the projection of the traction in the direction of the motion, i.e., tangent to the interface having normal $\boldsymbol{n}$ (note that where the interface is roughly normal to the y-axis, $(S_{xy})_1/(S_{xy})_2 \approx K$). This constraint impacts the velocity field, resulting in an increment of the velocity within the central stream (Fluid 1) as previously displayed in Figure 8, which, in turn, results in a contraction of the central stream in order to satisfy the incompressibility requirements. Analogous considerations apply to the case for $AR = 0.22$ (Figure 16b), where only the contours for the shear component S_{xy} are shown. In this case, it can be observed that for $K = 1$ the interface is almost straight, reflecting the fact that the stresses generated at the walls have a negligible impact on it due to the larger relative distance over which these are produced compared to the case $AR = 0.84$. It can be noted, in fact, that for the case $AR = 0.22$, shear stresses next to the interface are vanishingly small, while, on the contrary, for the corresponding $AR = 0.84$ situation these are non-negligible in the region of the interface.

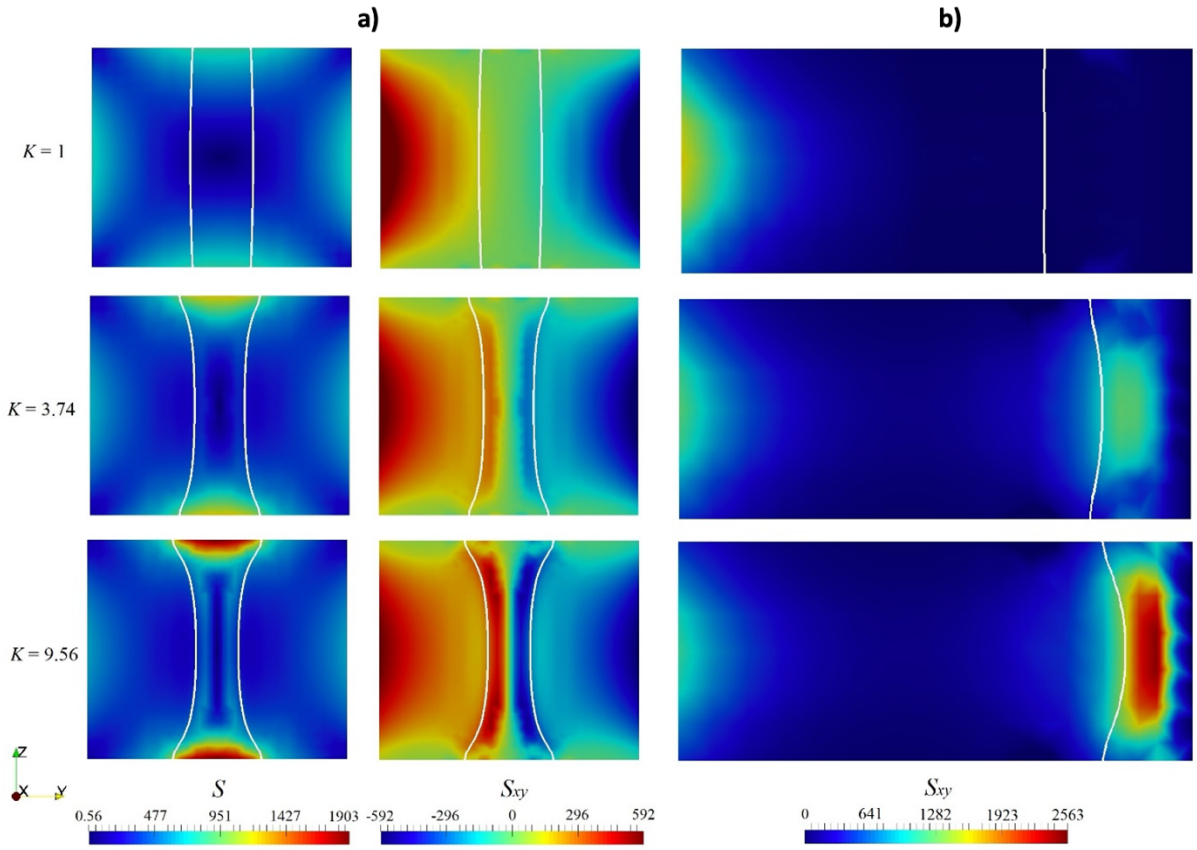

FIG 16. a) Contours of the magnitude of the rate-of-strain tensor, S, and its shear component, S_{xy}, observed in the y-z plane in the flow focusing geometry with $AR = 0.84$ and , $VR = 1$ and three viscosity ratios $K = 1, 3.74, 9.56$ for full channel depth ($0 < z/D < 1$) at location $x/W = 2.5$. b) Contours for the S_{xy} component for the case $AR = 0.22$ (only half of the domain is shown) for the same conditions in (a). Solid white lines showing the location of the interface are superimposed to each image.

The shape of the central focused stream was further investigated numerically by varying the viscosity ratio within a channel of aspect ratio 0.22 (Figure 17).

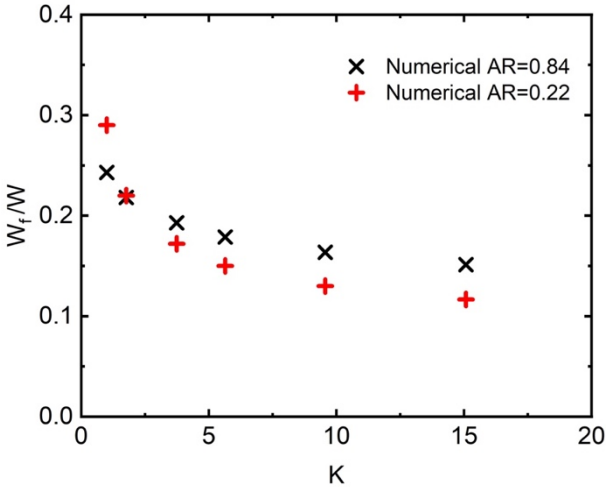

FIG 17. Impact of viscosity ratio on the central focused outlet stream in flow focusing geometries at the centre plane for $VR = 1$. Comparison of the normalised width of the focused stream for increasing values of K obtained from 3D numerical simulations for $AR = 0.84$ and $AR = 0.22$.

As the channel aspect ratio is reduced to $AR = 0.22$, similar trends to those obtained for the case $AR = 0.84$ are observed for increasing values of K with regards to the decreasing dimensionless filament width at the centre plane (c.f. Figure 17) and changing interfacial shape across the channel cross-section (c.f. Figure 14b). However, if we consider the average width ($\overline{W}_f$) of the central outlet stream along the whole depth of the channel (cf. Figure 18), we can see that for the aspect ratio of 0.84 the average width varies only slightly with K (similarly to the 2D analytical solution) however, as expected, for the aspect ratio of 0.22, the average value varies significantly with K, highlighting that confinement plays a significant role in the development of 3D viscous effects.

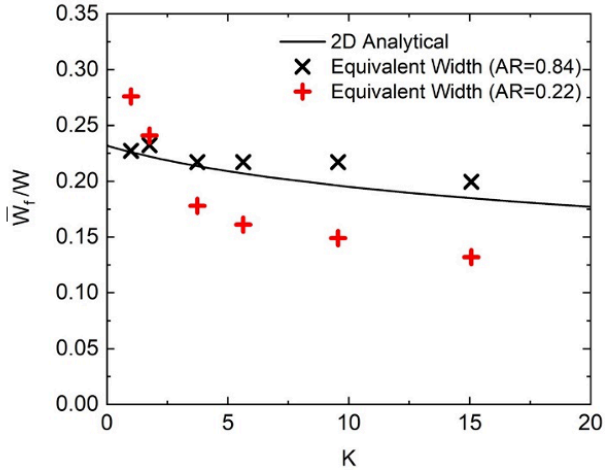

FIG 18. Impact of viscosity ratio on the central focused outlet stream for $VR = 1$ comparing the normalised width obtained via the 2D analytical solution with the normalised width averaged along the cross-section obtained in the simulations for $AR = 0.84$ and $AR = 0.22$.

VIII. CONCLUSIONS

In this work, a series of experiments and three-dimensional numerical simulations were carried out considering a microfluidic flow focusing device to investigate the impact of flow parameters influencing the characteristics of the produced central focused stream. Hydrodynamic focusing was induced using three fluid inlets (two lateral streams and a central stream of miscible Newtonian fluids). Specifically, we investigated the effect of the viscosity ratio, K, considering a relatively wide range of conditions ($1 \leq K \leq 15.07$), while simultaneously considering the combined effect of different velocity ratios ($1 < VR < 20$) and aspect ratio on the characteristics of the outlet central focused stream. An increase of the velocity ratio brings about a reduction of the width of the central focused stream at the centre plane ($z = D/2$) and enhances the curvature of the separation streamlines in agreement with previous work (Nguyen and Huang 2005, Oliveira et al. 2012). Under these conditions the viscous stresses from the lateral fluid streams dominate how the central fluid profile is formed. We have also derived a two-dimensional analytical expression, which is in agreement with 2D numerical results and provides a

good estimate of the findings for the configuration with aspect ratio $AR = 0.84$. As the microchannel becomes shallower, i.e. D becomes progressively smaller than W, the two-dimensional analytical solution provides less accurate estimations, and the experimental values are better captured by the analytical solution proposed by Wu and Nguyen (Wu and Nguyen, 2005) in the Hele-Shaw limit. The results obtained provide further insight into the curved interface along the channel depth that has been observed in previous research when high viscosity contrasts are present in parallel flow systems (Knight et al. 1998, Cubaud and Mason 2008, Cubaud et al. 2012, Cubaud and Mason 2012). Results confirm that a jump in stresses at the interface between the two fluids influences the concave shape of the interface along the depth of the channel cross-section. It was observed that the curved shape across the depth of the channel cross-section (i.e. along the z-direction) is strongly dependent on the viscosity ratio and aspect ratio, highlighting that confinement also plays an important role in the development of three-dimensional viscous effects.

ACKNOWLEDGEMENTS

Oliveira and Houston acknowledge PhD studentship funding from EPSRC (Project reference 1960606) and Ronald Miller Foundation.

AUTHORS' DECLARATIONS

Conflicts of interest

The authors have no conflicts of interest to disclose.

Data availability

The data that support the findings of this study are available from the corresponding author upon reasonable request.

REFERENCES

Anna, S. L., Bontoux, N. and Stone, H. A. (2003). "*Formation of dispersions using "flow focusing" in microchannels.*" **Applied Physics Letters 82**(3): 364-366

Ateya, D. A., Erickson, J. S., Howell, P. B., Jr., Hilliard, L. R., Golden, J. P. and Ligler, F. S. (2008). "*The good, the bad, and the tiny: a review of microflow cytometry.*" **Anal Bioanal Chem 391**(5): 1485-1498

Bonhomme, O., Morozov, A., Leng, J. and Colin, A. (2011). "*Elastic instability in stratified core annular flow.*" **Phys Rev E Stat Nonlin Soft Matter Phys 83**(6 Pt 2): 065301

Capobianchi, P., Lappa, M. and Oliveira, M. S. N. (2017). "*Walls and domain shape effects on the thermal Marangoni migration of three-dimensional droplets.*" **Physics of Fluids 29**(11)

Cubaud, T. (2020). "*Swelling of Diffusive Fluid Threads in Microchannels.*" **Phys Rev Lett 125**(17): 174502

Cubaud, T., Jose, B. M., Darvishi, S. and Sun, R. (2012). "*Droplet breakup and viscosity-stratified flows in microchannels.*" **International Journal of Multiphase Flow 39**: 29-36

Cubaud, T. and Mason, T. G. (2006). "*Folding of viscous threads in diverging microchannels.*" **Phys Rev Lett 96**(11): 114501

Cubaud, T. and Mason, T. G. (2008). "*Capillary threads and viscous droplets in square microchannels.*" **Physics of Fluids 20**(5)

Cubaud, T. and Mason, T. G. (2008). "*Formation of miscible fluid microstructures by hydrodynamic focusing in plane geometries.*" **Phys Rev E Stat Nonlin Soft Matter Phys 78**(5 Pt 2): 056308

Cubaud, T. and Mason, T. G. (2012). "*Interacting viscous instabilities in microfluidic systems.*" **Soft Matter 8**(41)

Cubaud, T., Tatineni, M., Zhong, X. and Ho, C. M. (2005). "*Bubble dispenser in microfluidic devices.*" **Phys Rev E Stat Nonlin Soft Matter Phys 72**(3 Pt 2): 037302

d'Olce, M., Martin, J., Rakotomalala, N., Salin, D. and Talon, L. (2009). "*Convective/absolute instability in miscible core-annular flow. Part 1: Experiments.*" **Journal of Fluid Mechanics 618**: 305-322

Daniele, M. A., Boyd, D. A., Adams, A. A. and Ligler, F. S. (2015). "*Microfluidic strategies for design and assembly of microfibers and nanofibers with tissue engineering and regenerative medicine applications.*" **Adv Healthc Mater 4**(1): 11-28

Davoodi, M., Houston, G., Downie, J., Oliveira, M. S. N. and Poole, R. J. (2021). "*Stabilization of purely elastic instabilities in cross-slot geometries.*" **Journal of Fluid Mechanics 922**

Garstecki, P., Stone, H. A. and Whitesides, G. M. (2005). "*Mechanism for flow-rate controlled breakup in confined geometries: a route to monodisperse emulsions.*" **Phys Rev Lett 94**(16): 164501

Golden, J. P., Justin, G. A., Nasir, M. and Ligler, F. S. (2012). "*Hydrodynamic focusing--a versatile tool.*" **Anal Bioanal Chem 402**(1): 325-335

Guillot, P., Panizza, P., Salmon, J.-B., Joanicot, M. and Colin, A. (2006). "*Viscosimeter on a Microfluidic Chip.*" **Langmuir 22**: 6438-6445

Hooper, A. P. and Boyd, W. G. C. (2006). "*Shear-flow instability at the interface between two viscous fluids.*" **Journal of Fluid Mechanics 128**(-1)

Hu, X. and Cubaud, T. (2016). "*Inertial destabilization of highly viscous microfluidic stratifications.*" **Physical Review Fluids 1**(4)

Joseph, D. D., Nguyen, K. and Beavers, G. S. (1984). "*Non-uniqueness and stability of configuration of flow of immiscible fluids with different viscosities.*" **Journal of Fluid Mechanics 141**: 319-345

Jun, Y., Kang, E., Chae, S. and Lee, S. H. (2014). "*Microfluidic spinning of micro- and nano-scale fibers for tissue engineering.*" **Lab Chip 14**(13): 2145-2160

Knight, J. B., Vishwanath, A., Brody, J. P. and Austin, R. H. (1998). "*Hydrodynamic Focusing on a Silicon Chip: Mixing Nanoliters in Microseconds.*" **Physical Review Letters 80**(17)

Lan, W., Li, S., Lu, Y., Xu, J. and Luo, G. (2009). "*Controllable preparation of microscale tubes with multiphase co-laminar flow in a double co-axial microdevice.*" **Lab Chip 9**(22): 3282-3288

Lee, G.-B., Chang, C.-C., Huang, S.-B. and Yang, R.-J. (2006). "*The hydrodynamic focusing effect inside rectangular microchannels.*" **Journal of Micromechanics and Microengineering 16**(5): 1024-1032

Lee, G.-B., Hung, C.-I., Ke, B.-J., Huang, G.-R., Hwei, B.-H. and Lai, H.-F. (2001). "*Hydrodynamic Focusing for a Micromachined Flow Cytometer.*" **Journal of Fluids Engineering 123**(3): 672-679

Nguyen, N. T. and Huang, X. (2005). "*Mixing in microchannels based on hydrodynamic focusing and time-interleaved segmentation: modelling and experiment.*" **Lab Chip 5**(11): 1320-1326

Oliveira, M., Pinho, F. T. and Alves, M. A. (2011). Extensional Flow of Newtonian and Boger Fluids Through a Flow Focusing Microdevice. 3rd Micro and Nano Flows Conference. Thessaloniki, Greece.

Oliveira, M. S. N., Alves, M. A., Pinho, F. T. and McKinley, G. H. (2007). "*Viscous flow through microfabricated hyperbolic contractions.*" **Experiments in Fluids 43**(2-3): 437-451

Oliveira, M. S. N., Pinho, F. T. and Alves, M. A. (2012). "*Divergent streamlines and free vortices in Newtonian fluid flows in microfluidic flow-focusing devices.*" **Journal of Fluid Mechanics 711**: 171-191

Petitjeans, P. and Maxworthy, T. (1996). "*Miscible displacements in capillary tubes. Part 1. Experiments.*" **Journal of Fluid Mechanics 326**: 37-56

Sousa, P. C., Coelho, P. M., Oliveira, M. S. N. and Alves, M. A. (2009). "*Three-dimensional flow of Newtonian and Boger fluids in square–square contractions.*" **Journal of Non-Newtonian Fluid Mechanics 160**(2-3): 122-139

Ward, T., Faivre, M., Abkarian, M. and Stone, H. A. (2005). "*Microfluidic flow focusing: drop size and scaling in pressure versus flow-rate-driven pumping.*" **Electrophoresis 26**(19): 3716-3724

Wu, Z. and Nguyen, N.-T. (2005). "*Hydrodynamic focusing in microchannels under consideration of diffusive dispersion: theories and experiments.*" **Sensors and Actuators B: Chemical 107**(2): 965-974

Yih, C.-S. (1967). "*Instability due to viscosity stratification.*" **Journal of Fluid Mechanics 27**(2): 337-352